Supplementary information:

Controlled lateral anisotropy in correlated manganite heterostructures by interface-engineered oxygen octahedral coupling

Z. Liao[1], M. Huijben[1*], Z. Zhong[2], N. Gauquelin[3], S. Macke[4,5], R. Green[4,6], S. van Aert[3], J. Verbeeck[3], G. Van Tendeloo[3], K. Held[2], G. A. Sawatzky[4], G. Koster[1] & G. Rijnders[1]

[1]*MESA+ Institute for Nanotechnology, University of Twente, P.O.BOX 217, 7500 AE, Enschede, The Netherlands*

[2]*Institute of Solid State Physics, Vienna University of Technology, A-1040 Vienna, Austria*

[3]*Electron Microscopy for Materials Science (EMAT), University of Antwerp, 2020 Antwerp, Belgium*

[4]*Quantum Matter Institute and Department of Physics and Astronomy, University of British Columbia, 2355 East Mall , Vancouver, V6T 1Z4 , Canada*

[5]*Max Planck Institute for Solid State Research, Heisenbergstraße 1, 70569 Stuttgart, Germany*

[6]*Max Planck Institute for Chemical Physics of Solids, Nöthnitzerstraße 40, 01187 Dresden, Germany*

1. Growth of $La_{2/3}Sr_{1/3}MnO_3$ and $SrTiO_3$ films

The $La_{2/3}Sr_{1/3}MnO_3$ (LSMO) and $SrTiO_3$ (STO) films were grown by pulsed laser deposition (PLD) in a layer by layer fashion as shown in Figure S1a. The thickness of the LSMO and STO was controlled by counting the RHEED oscillations, enabling a precise unit cell (uc) control of the growth. The surface morphology was characterized by atomic force microscopy (AFM), which showed atomic flat surface of the LSMO films with clear one unit cell height terrace steps (see Figure S1b-c). RHEED pattern of a 30 uc LSMO film, as shown in the inset of Figure S1c, also indicates a 2D smooth surface.

* email: m.huijben@utwente.nl

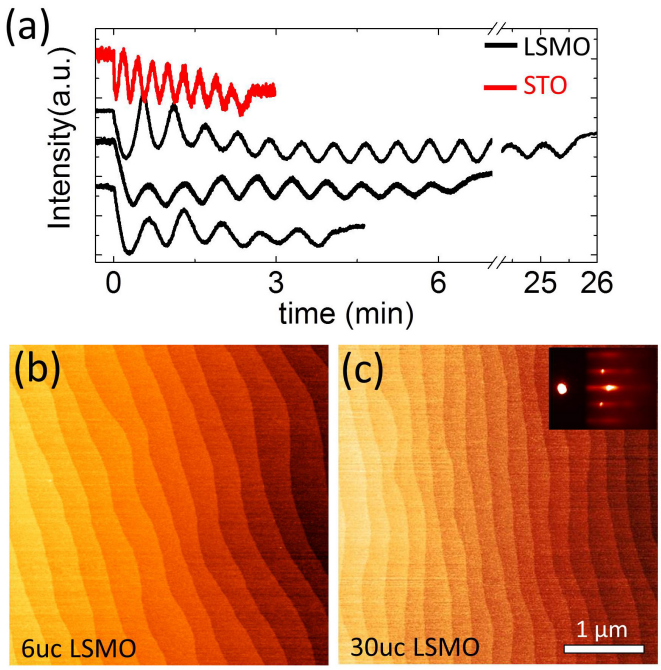

Figure S1 | Growth and characterization of LSMO and STO films. (a) RHEED intensity oscillations during the growth of LSMO (6, 10, 44 uc) and STO (9 uc). AFM images of 6 uc (**b**) and 30 uc (**c**) LSMO layers.

2. X-ray reciprocal space mapping of $La_{2/3}Sr_{1/3}MnO_3$ and $SrTiO_3$ films

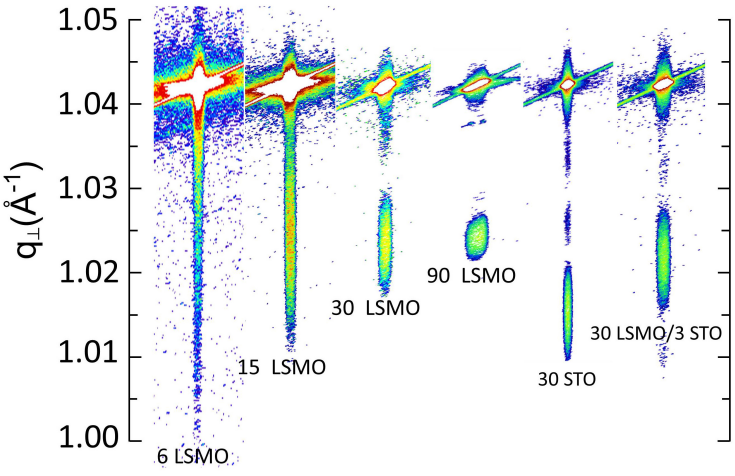

Figure S2 | X-ray reciprocal space mapping of (620) peaks for different thicknesses (6, 15, 30, 90 uc) of LSMO films, 30 uc STO and 30 uc LSMO with 3 uc STO buffer layer on $NdGaO_3$ (110) substrates. The thickness in unit of unit cell is indicated near the peak.

Due to a very small lattice mismatch (0.4%) between the LSMO and NGO crystal structures, the LSMO layer is easily strained to the NGO substrate as confirmed by X-ray diffraction (XRD) measurements, which were performed using a PANalytical X'Pert Materials Research Diffractometer (MRD) in high resolution mode. Reciprocal space mapping (RSM) of (260), (444), (620) and (44-4) diffraction peaks has been performed at room temperature. Figure S2 only shows (620) peaks as examples. According to RSM, the LSMO films ranging from 4 unit cell (uc) to 90 uc have same in-plane lattice constants with $NdGaO_3$ (NGO) substrates, indicating that all films are fully strained to the substrates regardless of film thickness. The STO buffer layer is fully strained to the NGO substrate as indicated by the RSM of a 30 uc STO film on a NGO substrate. For STO-buffered LSMO, it is found that the LSMO layers are still fully strained to the NGO substrates. Therefore, with or without STO buffer layer, the in-plane lattice constants (*a* and *b*) of LSMO maintain constant.

3. Interfacial Energy-dispersive X-ray spectroscopy (EDX) maps and estimation of oxygen octahedral tilt angle

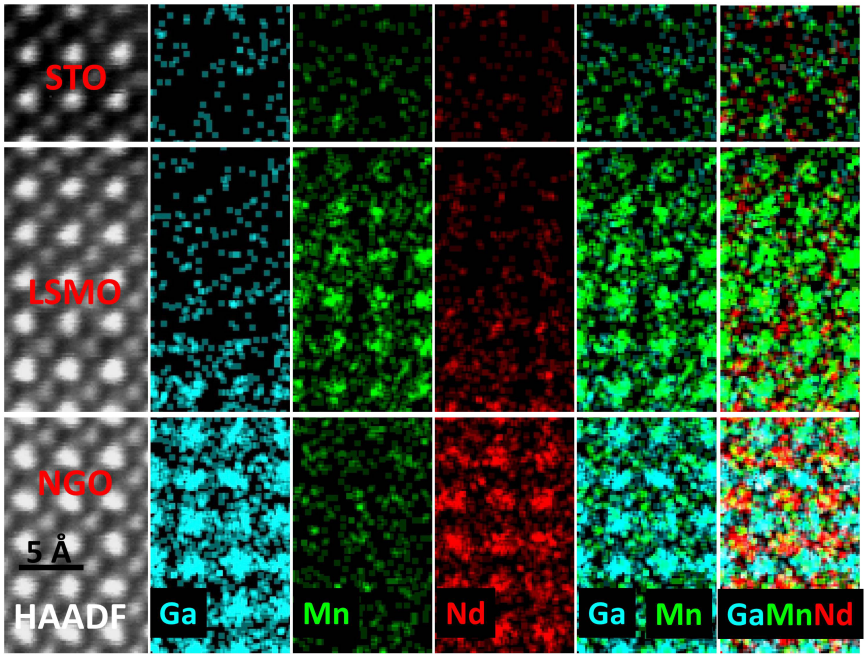

Figure S3 | Atomic resolution EDX mapping of Mn, Ga and Nd at the LSMO/NGO interface.

The interfacial atomic ordering in LSMO/NGO heterostructures is determined by performing EDX mapping across the interface. The LSMO film was capped with a 10 nm $SrTiO_3$ (STO) layer in order to prevent LSMO ultrathin layer from damage during the preparation of transmission electron microscopy (TEM) cross-section specimen. The STO overlayer was grown at room temperature. However, some crystalline STO islands were formed at interface. The capping by room temperature grown STO did not affect the magnetic properties of the underlying LSMO film. An example of atomic EDX mapping of Mn, Ga and Nd is shown in Figure S3 and enables the characterization of the atomic ordering of MnO_6 and GaO_6 in the interface region. The presence of signal of Ga in the first MnO_2 layer in the EDX elemental maps, may come from the automatic drift correction applied by the acquisition software or secondary X-Rays. As the intensity in the Mn map in this layer is similar to the subsequent layers (containing no Ga), we can conclude that the amount of Ga diffusion in the LSMO film is negligible in agreement with the RXR results, as shown in Fig. 2d in the main text.

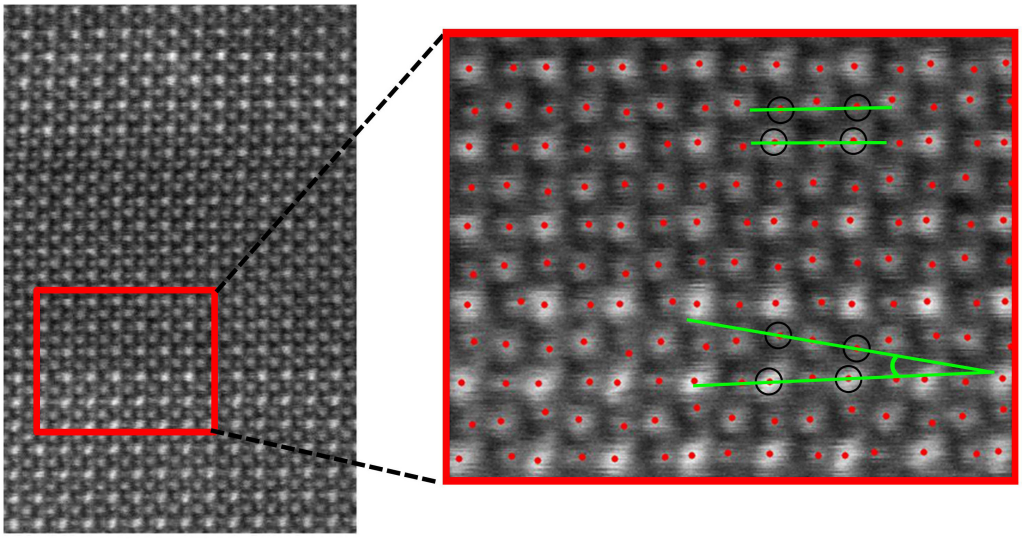

Figure S4 | Estimation of the oxygen octahedral tilt angle. Inversed ABF-STEM image of a LSMO/STO/NGO samples (left) and its enlarged view of the boxed region (right). The STO and LSMO are 9 uc and 6 uc thick, respectively. Small red dots are estimated atomic columns positions.

To study the layer-position dependent octahedral tilt angle, inversed Annular Bright-Field scanning transmission electron microscopy (ABF-STEM) images as indicated in Figure

S4 as an example have been quantified by statistical parameter estimation theory. Using this method, the experimental image intensities are modelled by a superposition of Gaussians functions peaked at the atomic column positions. The parameters of this model, including the atomic column positions, the height and width of the Gaussian peaks, have been determined using the least squares estimator [1-3]. From the estimated atomic column positions, the BO_6 octahedral tilt angles (β) (B being either Ga, Ti or Mn depending on the layer) have been determined as illustrated in the inversed ABF image of the LSMO/STO/NGO cross-section in Figure S4. From the estimated atomic column positions, shown in red dots in the right panel of Figure S4, the tilt of each octahedron has been determined by measuring the angle between two straight lines crossing pairs of heavy columns and pairs of light O columns. With this method, the layer position dependent mean values of these tilt angles together with their standard deviation on the mean have been determined and are shown Figure 1c in main text.

4. Magnetization architecture by engineering interfacial oxygen octahedral coupling

The capability to rotate the easy axis in-plane by controlled interface octahedral coupling allows us to realize non-collinear magnetization in a LSMO/STO/LSMO/NGO magnetic tunneling junction (MTJ). Figure S5a shows an example of a MTJ with orthogonal magnetic easy axes between top LSMO and bottom LSMO layers. As shown in Figure S5a, the M-H curve along [001]-axis of the LSMO/STO/LSMO/NGO MTJ is a combination of hard axis M-H curve from top LSMO layer and easy axis M-H curve from bottom LSMO layer. This scenario is confirmed when we fully removed the top LSMO layer by wet-etching with 20wt% HCl acid and measured the M-H again. The contribution to the total M-H curve from the bottom LSMO layer doesn't change after fully etching away the top LSMO layer. The M-H curve of the bottom LSMO layer also proves that it has an easy axis along [001] direction. By subtracting the magnetization of the bottom LSMO layer, we can extract the magnetization of the top LSMO layer (blue curve in Figure S5a), which shows a typical hard axis M-H characteristic. Therefore the easy axis for the top LSMO layer is along [1-10] direction.

By patterning the STO buffer layer, we are able to locally vary the magnetic properties. As shown in Figure S5b, we fabricated a patterned STO layer by using a shadow mask during growth. After in-situ removing the shadow mask, a 6 uc LSMO film was subsequently grown on the patterned STO layer. The M-H curve of such sample as shown in Figure S5b shows a typical combination of hard axis M-H curve from the LSMO/STO/NGO region and easy axis M-H curve from the LSMO/NGO region.

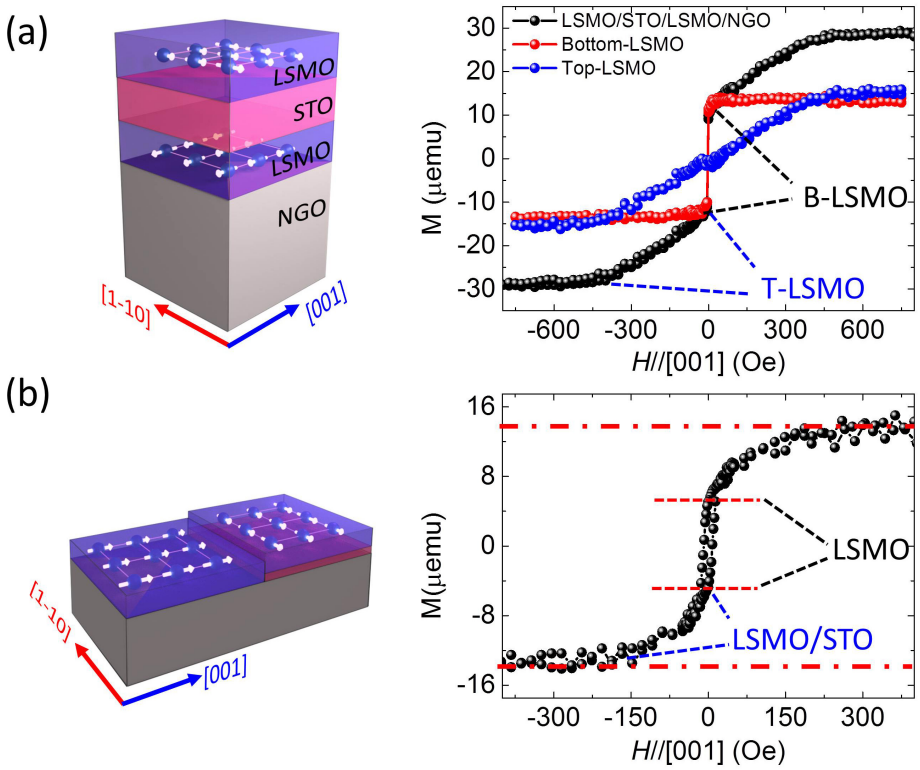

Figure S5 | Magnetization architecture in out of plane and in-plane directions. a, Orthogonal magnetization in LSMO(6uc)/STO(8uc)/LSMO(6uc)/NGO magnetic tunneling junction**.** Left, the schematic spin configuration of bottom LSMO (B-LSMO) and top LSMO (T-LSMO) layers. Right, M-H curves along [001] axis for as-grown (AG) sample (black curve), and top LSMO fully etched (TLE) sample (red curve) and extracted magnetization of top LSMO layer (green curve) by subtracting TLE from AG (AS-TLE). The M-H curves were measured at 150 K. **b**, In-plane magnetization patterning. Left panel shows the LSMO film on patterned STO buffer layer. The STO buffer layer (red) in left panel is 1 uc thick and the LSMO film (blue) is 6 uc thick everywhere. Right panel shows the M-H curve along [001] direction at 75 K.

5. Determination of the magneto-optical profile of Mn

The magneto-optical profile was determined by x-ray resonant magnetic reflectivity (XRMR) [4]. An element-specific continuum model was used to construct an energy and depth dependence refractive index [5]. The optical constants of Mn, La and Nd were taken from XAS signals and fitted to off-resonant tables, and for all other elements the tabulated values were used [6].

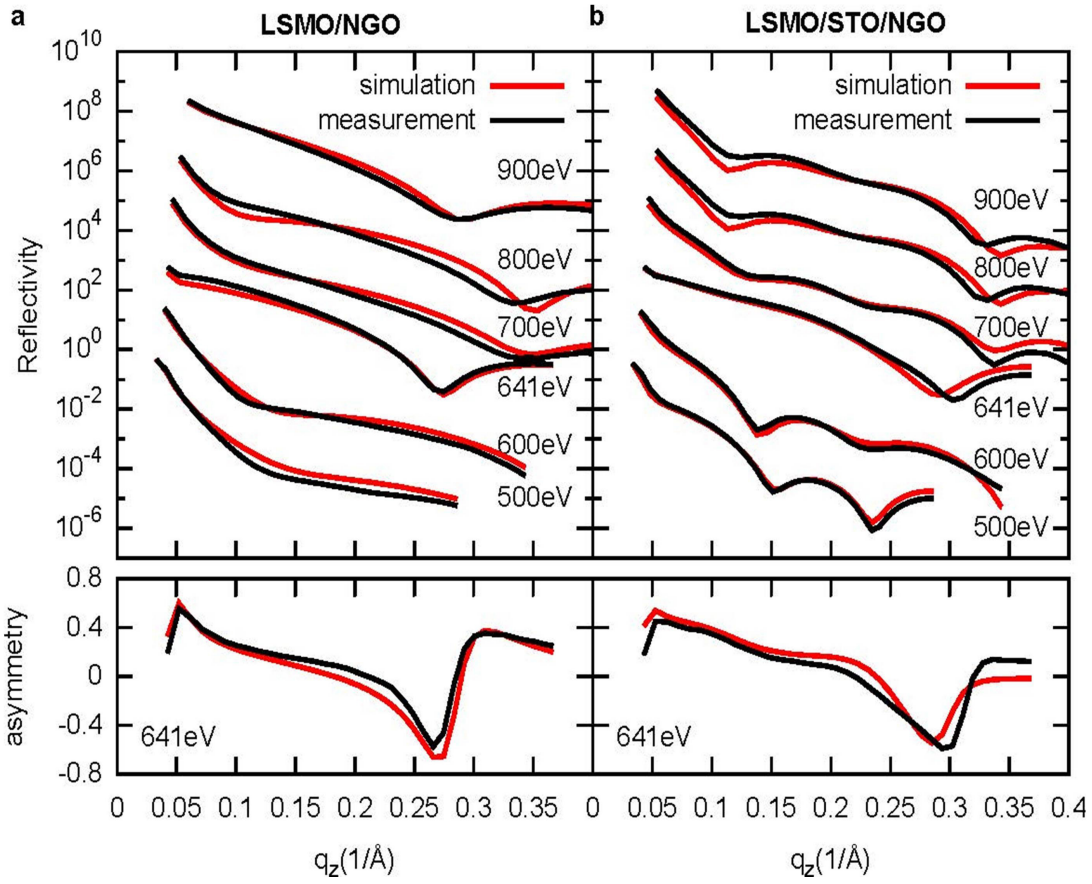

Figure S6 | Measured and simulated reflectivity curves for LSMO/NGO (a) and LSMO/STO/NGO (b) at 20 K. The structural fit was performed using the off-resonant energies. For clarity the reflectivity curves are scaled. The magnetic profile (bottom) was determined on the L_3 edge of Mn at 641 eV by the asymmetry signal between left and right circular polarized light with an applied magnetic field along the scattering plane.

The chemical depth profile is determined using reflectivity curves measured at off-resonant energies, utilizing the optical contrast before and after each resonance. The film thickness, roughness, and a small contamination of light elements were taken as fit

parameters, while the concentrations of the NGO, STO, and LSMO elements were fixed at stoichiometric values. Figure S6 shows the corresponding measurements and fits, which were performed using the software ReMagX [6,7]. Soft X-Ray Reflectivity of a 6 uc LSMO film with and without a STO buffer layer shows similar behavior to hard X-Ray Reflectivity, strongly indicating the high quality of our LSMO and STO films.

After determining the chemical profile, further measurements and modeling were used to determine the magneto-optical depth profile. For these measurements, a permanent magnet array producing a homogenous 0.6 Tesla field was inserted in the sample environment, aligning the magnetization in the film xy plane along the measurement scattering plane. Two different reflectivity curves at the Mn L_3 resonance were measured by using left R_l and right circular R_r polarized light. Figure S6 (bottom) shows the asymmetry defined as $A = (R_l-R_r)/(R_l+R_r)$ and the corresponding fit. During fitting, the magnetic depth profile was assumed to be one homogeneous magnetic layer with in-plane magnetization and free thickness, position and magnetic roughness. As model inputs, the magneto optical constants were determined by the XMCD spectra taken from [8].

The magnetic profile obtained from XRMR is consistent with magnetization measured by Quantum Design Vibrating Sample Magnetometer (QD-VSM). At 50 K, the saturated magnetic moment from VSM for a 6 uc LSMO film with a 9 uc STO buffer layer is 2.29 μ_B/Mn while for a non-buffered 6 uc LSMO film it is 1.57 μ_B/Mn, so their ratio is 1.46. Comparing with the estimated ratio of ~1.43 from the magnetic profile, as shown in Fig. 2d in main text, they are self-consistent.

5. Characterization of transport properties

A van-der-Pauw geometry, as shown in Figure S7a, is utilized to measure the anisotropic transport properties [9]. The $R_{[001]} = V_{24}/I_{13}$ and $R_{[1\text{-}10]} = V_{12}/I_{34}$ are simultaneously measured during the temperature variations. As shown in Figure S7b**,** the T_P in temperature dependent the MR curve increases with increasing thickness. The LSMO film with higher T_P exhibits a lower MR effect. The maximum |MR|, which occurs at T_p, decreases with increasing T_P. The Curie temperature (T_C) also increases with increasing

thickness, see Figure S7c. T_C and T_P for a specific LSMO film are almost equal, hence T_P in transport behavior can very well reflect the magnetic phase transition and metal-insulator transition (MIT) in LSMO. It can be concluded that the LSMO film with higher magnetization will have a lower MR effect.

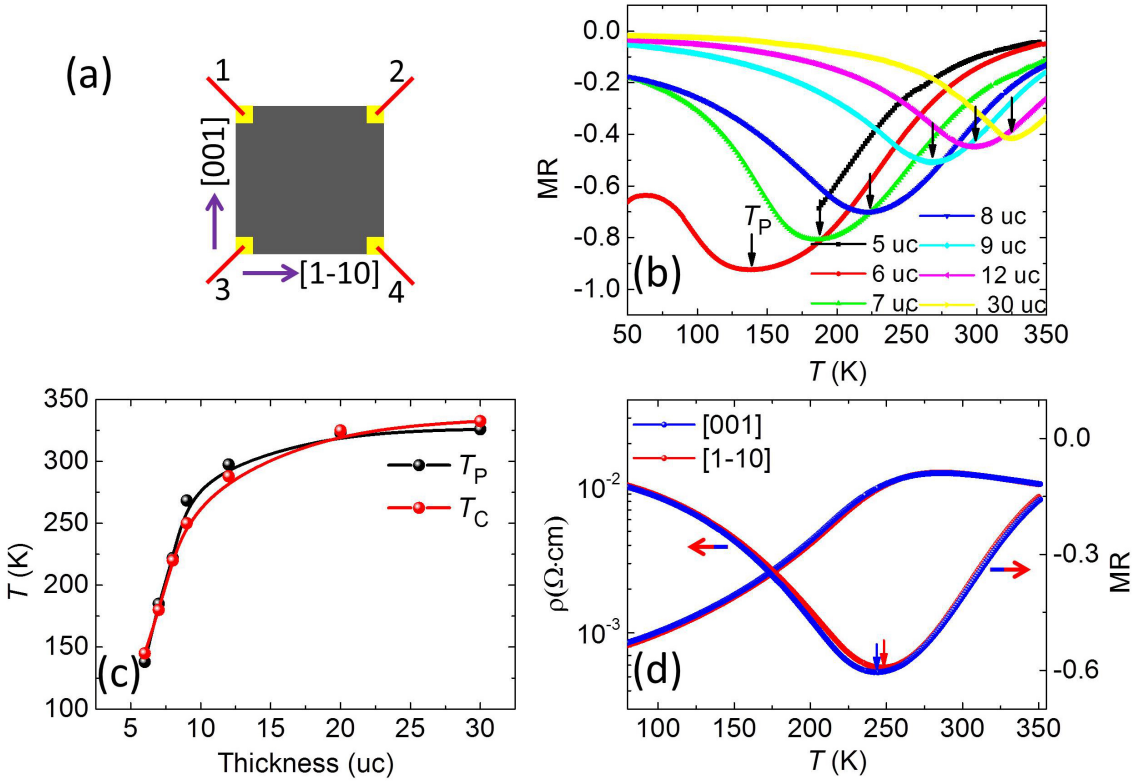

Figure S7 | Electrical characterization of LSMO thin films. a, Schematic of the resistivity measurement by van-der-Pauw geometry with four 0.5 mm × 0.5 mm gold electrodes at corners. The sample size is 5 mm x 5 mm. **b**, Temperature dependent $MR_{[001]}$ ($\equiv$($R_{[001]}$(9 T)-$R_{[001]}$ (0 T))/$R_{[001]}$ (0 T)) for LSMO films with different thicknesses under out of plane 9 T magnetic field. **c**, Thickness dependent T_C and T_P of LSMO films on NGO substrates. (d) Temperature dependent resistivity and magnetoresistance MR=(R(B)-R(0))/R(0) along [001] and [1-10] for LSMO(6uc)/STO(9uc)/NGO sample. The MR was measured under out of plane 9 T magnetic field.

For a STO-buffered LSMO film, which behaves similar as a strain-dominated thick LSMO film, the transport anisotropy is very small as shown in Figure S7d. The STO buffered 6 uc LSMO film is more conductive than the non-buffered 6 uc LSMO film

(data shown in Figure 4a in main text), consistent with the enhanced magnetism as mentioned in main text. The STO buffered 6 uc LSMO film exhibits very weak transport anisotropy. According to the temperature dependent MR curve, as shown in Figure S7d, the MR along [1-10] direction has a higher T_P, consistent with it's magnetic easy axis of [1-10].

6. Calculation of mean anisotropic energy constant from M-H curves

For uniaxial magnetic anisotropy, the magnetic anisotropy energy can be described by $E = K_u \cos^2\varphi$ where φ is an in-plane angle relative to *a*-axis and K_u is the anisotropy energy constant. Here we neglect higher order terms. By measuring the field dependent magnetization M-H curve along the hard axis, to obtain H_K and M_S as shown in Figure S8, the K_u can be determined by formula $K_u = H_k \cdot M_S/2$ [10].

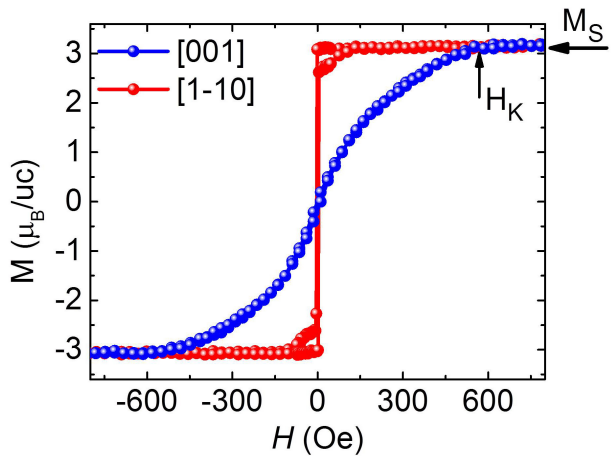

Figure S8 | M-H curves along two orthogonal directions taken at 100K for a 15 uc LSMO film on NGO (110) substrate. The arrows indicate the saturated magnetization M_S and switching field H_K where the magnetization starts to reach the saturated value M_S.

7. Density functional theory (DFT) based tight binding calculation of magnetic anisotropy energy

There are several sources of magnetic anisotropy, magnetocrystalline, shape, and exchange anisotropy. Since NGO and STO are not magnetic, we can exclude the exchange anisotropy with the substrate. Shape anisotropy is, on the other hand, only affecting the out-of-plane anisotropy, not the in-plane *a*- vs. *b*-axis anisotropy, which is at the focus of our study. From microscopic measurements of the Ga and Mn profiles, as shown in Fig. 2d of main text, a chemically very sharp interface was concluded. Intermixing at the interface between LSMO and NGO is negligible. Although we cannot fully exclude very small amounts of inter-diffusion at the interface, the non-magnetic Ga would not contribute to the magnetic anisotropy. This leaves us with magnetocrystalline anisotropy, which is an intrinsic property of a ferromagnet. It depends on the crystal structure, but is independent of grain size and shape. The magnetic easy/hard axis of our LSMO ultrathin films on NGO is along a specific crystalline orientation such as [001] and [1-10] and, as we will show, can even be tuned by structural changes such as inserting an STO buffer layer or increasing thickness. Magnetocrystalline anisotropy can hence be expected to play the dominant role for the observed magnetic anisotropy.

The magnetocrystalline anisotropy originates from the spin-orbit coupling and can be qualitatively calculated by a tight-binding approach and perturbation analysis [11, 12]. To obtain a more realistic description for various materials, first principles density functional theory (DFT) calculations are desirable [13]. However, the magnetic anisotropy energy (MAE) (e.g. of LSMO ultrathin films in our study) is usually of the order of 1μeV/uc, which is much weaker than the exchange interaction of 1eV and is hence difficult to compute from DFT with sufficient numerical accuracy. A DFT based tight-binding Hamiltonian can overcome this problem and produce sub μeV precision [14].

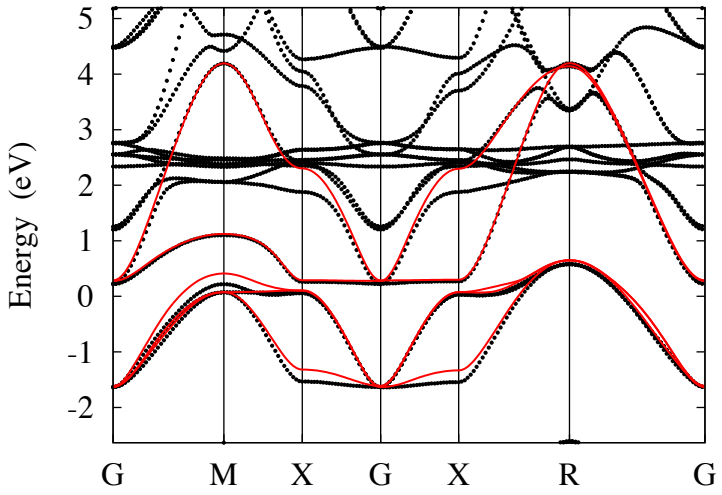

Figure S9 | DFT band structure (black) for 0.3% extensive stained $LaMnO_3$ and the tight binding band structure from Wannier projection (red). The small discrepancy arises from the entanglement of Mn e_g bands with other bands.

We hence construct a DFT-based tight-binding Hamiltonian, $H(\vec{k}) + \left(\frac{\lambda}{2}\right)\sigma(\theta,\varphi) + \xi L \cdot S$, to calculate the MAE of LSMO ultrathin films. Here, the first term, $H(\vec{k})$, is the paramagnetic tight-binding Hamiltonian, constructed in the Wannier basis, which in turn was obtained from the projection of DFT-calculated Bloch waves of LSMO near the Fermi level. It has matrix elements $H_{\alpha\beta}(\vec{k}) = \sum_R t_{\alpha\beta}(\vec{R})\, e^{i\vec{K}\cdot\vec{R}}$ where $\vec{R}$ denotes lattice sites, α and β denote orbitals in Wannier basis with Mn d (d_{xy}, d_{yz}, d_{xz}, d_{z^2}, $d_{x^2-y^2}$) orbitals characters, $t_{\alpha\beta}(\vec{R})$ represents a hopping integral from orbital α at site 0 to orbital β at site $\vec{R}$, and k is the wave vector. For the DFT calculation we used the Wien2K package [15] with the PBE potential. The Wannier projection was performed with Wien2Wannier package [16], which employs Wannier90 for constructing maximally localized Wannier orbitals [17], for more details see Ref. [18]. We have performed the DFT calculation and Wannier function projection for both, cubic and 0.5% extensive strain. Figure S9 compares the Wannier bands with DFT for the latter case, where we get an anisotropy parameter (defined in the main text) A_t=0.6%.

The second term $\left(\frac{\lambda}{2}\right)\sigma(\theta,\varphi)$ describes an exchange splitting λ with magnetization along the direction (θ, φ), where σ(θ, φ) is the vector of Pauli matrices times a unit vector in the

direction (θ, φ), so that a spin-up state in the (θ, φ)-direction has energy $+\frac{\lambda}{2}$ and a spin-down spin $-\frac{\lambda}{2}$. We employ λ = 2 eV which is the typical exchange splitting in manganites [19]. For the last term, the atomic spin orbit coupling of Mn *d* orbitals, we set ξ = 0.05 eV, a typical value for transition metals.

We diagonalize the Hamiltonian numerically and obtain the eigen-wavefunctions and eigen-energies $\varepsilon_i(k)$. Integrating over all *k* points in the first Brillouin zone, we obtain the total energy $E = \int_{BZ} \varepsilon_i(k)(\varepsilon_i - \varepsilon_F)dk$, where $f(\varepsilon_i\text{-}\varepsilon_F)$ is the Fermi-Dirac distribution at room temperature. The Fermi level ε_F is determined by the total number of d electrons per unit cell, i.e., n = 3.67 for $La_{2/3}Sr_{1/3}MnO_3$. Since the MAE of interest is of the order of 1 μeV/uc, we take advantage of the tight binding method and use a very fine *k* mesh (e.g. 160 × 160 × 160) to make sure that the total energy converges down to an accuracy of less than 10^{-3} μeV. Generally, the total energy, $E(\theta, \varphi)$, becomes a function of the magnetization orientation. In the absence of either magnetization (λ = 0) or spin-orbit coupling (ξ = 0), $E(\theta, \varphi)$ is constant. But for a ferromagnet (λ ≠ 0) with spin orbit coupling (ξ ≠ 0), it becomes energetically favorable if the magnetization points along a specific crystalline orientation, giving rise to magnetic anisotropy.

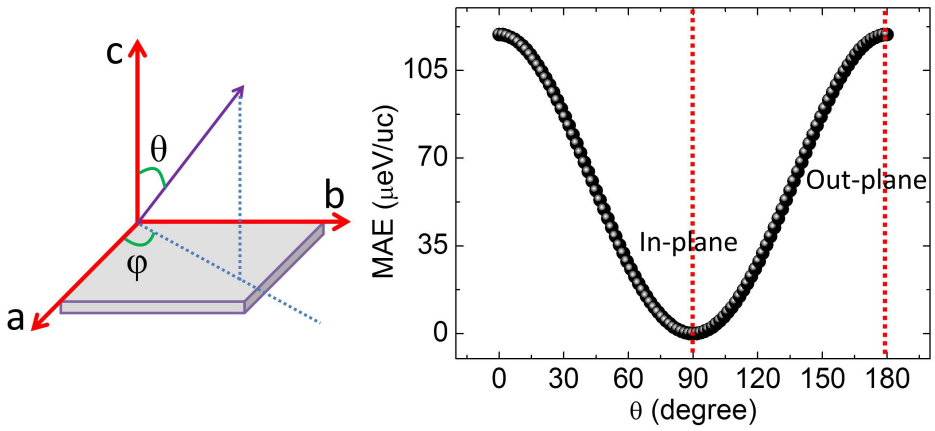

Figure S10 | DFT based tight binding calculation of MAE of single unit cell LSMO slab.

Figure S10 shows an example of the MAE as a function of θ for a free-standing monolayer LSMO film. The angle where MAE has its minimum defines the easy axis. In our case, we find that the easy axis lies in *ab* plane (θ = 90 degrees). Due to the reduced

symmetry, the out of plane MAE in thin films is strongly enhanced compared to that of the bulk [11-13]. The calculated energy scale of the out of plane MAE is ~0.1 meV/uc, quite consistent with the experimental values as mentioned above. Note that the shape anisotropy based on long-range dipole-dipole interactions can further modify this out of plane MAE [11]. The in-plane anisotropy (i.e., how the MAE depends on φ) is correlated to the asymmetric hopping factor A_t as described in main text. The in-plane anisotropic energy constant K is shown in Figure 5c of the main manuscript. It has an order of magnitude of 4 μeV/uc, consistent with experimental value.

8. Magnetic anisotropy of (001) LSMO films on cubic substrate

The (001) LSMO films grown on STO and $(LaAlO_3)_{0.3}(Sr_2AlTaO_6)_{0.7}$ (LSAT) both exhibit biaxial anisotropy with easy axis along $[110]_{pc}$ and $[1\text{-}10]_{pc}$ axis (pc represents pseudo-cubic index). The films were grown at same condition as films on NGO substrates. The LSMO films were coherently grown on these substrates as confirming by RSM of $(024)_{pc}$, $(0\text{-}24)_{pc}$, $(204)_{pc}$, $(\text{-}204)_{pc}$ peaks, hence the in-plane structure is isotropic. Figure S11 shows the M-H curves for a 30 uc LSMO films on (001) STO substrate along different crystal orientations at 100 K.

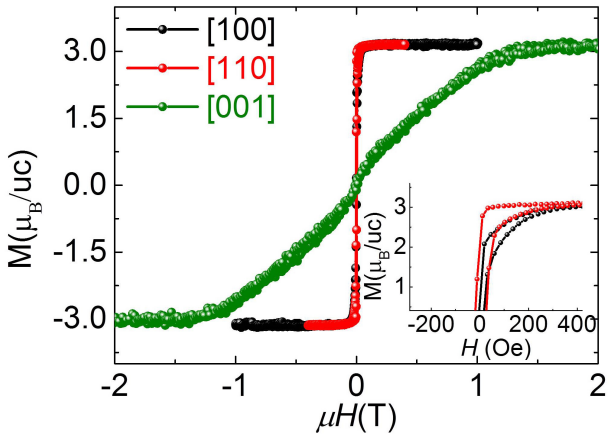

Figure S11 | Magnetic anisotropy of LSMO films on cubic STO (001) substrates at 100K. M-H curves of 30 uc LSMO film on STO (001) substrate along [100], [110] and [001] directions. Inset shows the zoom-in at low magnetic field region.

The in-plane easy axis is determined to be $[110]_{pc}$ and $[1\text{-}10]_{pc}$. The in-plane magnetic anisotropy constant K ($\equiv H_K \cdot M_S/2$) is 5.5 μeV/uc. For out of plane direction, the H_K is 1.4 T and accordingly K is 0.13 meV/uc. Similar values are obtained when growing LSMO films on cubic (001) LSAT substrates.

9. Characterization of magnetic properties

The magnetization (M) was measured by using a QD-VSM. Since the NGO substrate is paramagnetic, a linear magnetic field (H) dependent magnetization contributes to each M-H curve. The magnetization of the LSMO films was acquired by subtracting the paramagnetic signal of the NGO substrate. To precisely measure the magnetization of LSMO ultrathin films such as 6 unit cell (uc), a driven model of VSM was used to achieve a measurement error of ~3 x 10^{-7} emu, which corresponds to 0.03 μ_B/uc for a 6 uc thick LSMO sample with an area of 5 x 5 mm^2. An example of the measurement of a 15 uc LSMO is shown in Figure S12.

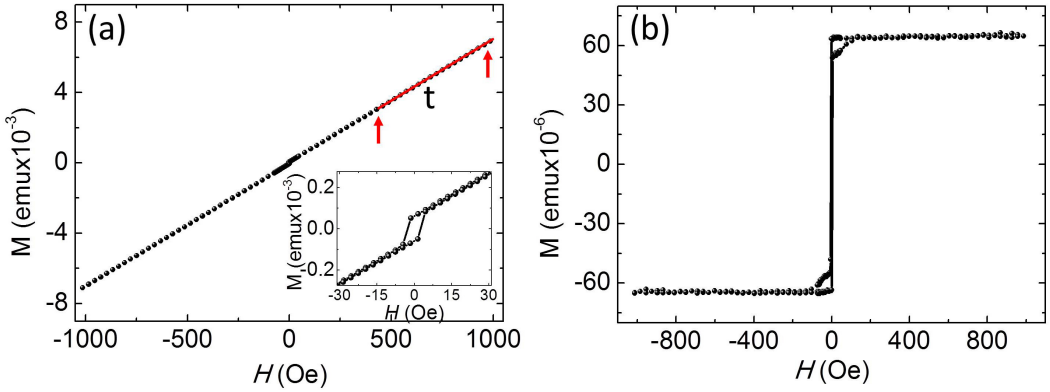

Figure S12 | Magnetic characterization of LSMO thin films. a, Raw measurement data of M-H curve of 15 uc LSMO film on NGO substrate at 100 K. Inset shows the zoom-in of low magnetic field region. **b**, Highly accurate M-H curve after subtracting the paramagnetic background signal of the NGO substrate.

The raw data in Figure S12a shows a hysteresis loop at low magnetic field, which originates from the ferromagnetic component of the LSMO film. By fitting the linear part at high field, a slope *t* is obtained and the NGO substrate signal can be removed from the

overall signal by formula M(film) = M(total) - t × H. An accurate M-H curve can now be obtained for each LSMO film as can be seen in Figure S12b.

References:

[1] A.J. den Dekker, S. Van Aert, A. van den Bos and D. Van Dyck, Maximum likelihood estimation of structure parameters from high resolution electron microscopy images. Part I: A theoretical framework, *Ultramicroscopy* **104**, 83 (2005).

[2] S. Van Aert, A.J. den Dekker, A. van den Bos, D. Van Dyck and J.H. Chen, Maximum likelihood estimation of structure parameters from high resolution electron microscopy images. Part II: A practical example, *Ultramicroscopy* **104**, 107 (2005).

[3] G.T. Martinez, A. Rosenauer, A. De Backer, J. Verbeeck and S. Van Aert, Quantitative composition determination at the atomic level using model-based high-angle annular dark field scanning transmission electron microscopy, *Ultramicroscopy* **137**, 12 (2014).

[4] S. Macke & E. Goering, Magnetic reflectometry of heterostructures, *Journal of Physics: Condensed Matter*, **26**, 363201, (2014).

[5] S. Macke, A. Radi, J.E. Hamann-Borrero, A. Verna, M. Bluschke, S. Brück, E. Goering, R. Sutarto, F.Z. He, G. Cristiani, E. Wu, E. Benckiser, H.U. Habermeier, G. Logvenov, N. Gauquelin, G.A. Botton, A.P. Kajdos, S. Stemmer, G.A. Sawatzky, M.W. Haverkort, K. Keimer, and V. Hinkov, Element specific monolayer depth profiling, *Adv. Mater.* **26**, 6554 (2014).

[6] C. Chantler, Theoretical form-factor, attenuation and scattering tabulation for Z=1-92 from E=1-10 eV to E=0.4-1.0 MeV, *Journal of Physical and Chemical Reference Data* **24**, 71 (1995).

[7] website: www.remagx.org.

[8] C. Aruta, G. Ghiringhelli, V. Bisogni, L. Braicovich, N.B. Brookes, A. Tebano, and G. Balestrino, Orbital occupation, atomic moments, and magnetic ordering at interfaces of manganite thin films, *Physical Review B* **80**, 014431 (2009).

[9] O. Bierwagen, R. Pomraenke, S. Eilers & W.T. Masselink, Mobility and carrier density in materials with anisotropic conductivity revealed by van der Pauw measurements, *Phys. Rev. B* **70**, 165307 (2004).

[10] B.D. Cullity, Introduction to magnetic materials, Addison-Wesley, Reading, Mass., (1972).

[11] P. Bruno, Tight-binding approach to the orbital magnetic moment and magnetocrystalline anisotropy of transition-metal monolayers, *Phys. Rev. B* **39**, 865 (1989).

[12] S. Pick & H. Dreysse, Monolayer magnetic anisotropy: A systematical tight-binding study, *Phys. Rev. B* **46**, 5802 (1992).

[13] G.H. O. Daalderop, P.J. Kelly & M.F.H. Schuurmans, First-principles calculation of the magnetocrystalline anisotropy energy of iron, cobalt, and nickel, *Phys. Rev. B* **41**, 11919 (1990).

[14] N. Marzari, A.A. Mostofi, J.R. Yates, I. Souza & D. Vanderbilt, Maximally localized Wannier function s: Theory and applications, *Rev. Mod. Phys.* **84**, 1419 (2012).

[15] P. Blaha, K. Schwarz, G.K.H. Madsen, D. Kvasnicka & J. Luitz, WIEN2k, An augmented plane wave + local orbitals program for calculating crystal properties, Karlheinz Schwarz, Techn. Universitat, Wien, Austria, 2001.

[16] J. Kunes, R. Arita, P. Wissgott, A. Toschi, H. Ikeda & K. Held, Wien2wannier: From linearized augmented plane waves to maximally localized Wannier functions, *Comp. Phys. Comm.* **181**, 1888 (2010).

[17] A.A. Mostofi, J.R. Yates, Y.-S. Lee, I. Souza, D. Vanderbilt & N. Marzari, Wannier90: A tool for obtaining maximally-localized Wannier functions, *Comp. Phys. Comm.* **9**, 685 (2008).

[18] Z. Zhong, A. Toth & K. Held, Theory of spin-orbit coupling at $LaAlO_3/SrTiO_3$ interfaces and $SrTiO_3$ surfaces, *Phys. Rev. B* **87**, 161102 (2013).

[19] A. Yamasaki, M. Feldbacher, Y.-F. Yang, O.K. Andersen & K. Held, Pressure-induced metal-insulator transition in $LaMnO_3$ is not of Mott-Hubbard type, *Phys. Rev. Lett.* **96**, 166401 (2006).